LBNL-41656
Preprint

ERNEST ORLANDO LAWRENCE
BERKELEY NATIONAL LABORATORY

Neutron Yields from 155 MeV/Nucleon C and He Stopping in Al

L. Heilbronn, R.S. Cary, M. Cronqvist, F. Deák,
K. Frankel, A. Galonsky, K. Holabird, Á. Horvath,
Á. Kiss, J. Kruse, R.M. Ronningen, H. Schelin, Z. Seres,
C.E. Stronach, J. Wang, P. Zecher, and C. Zeitlin

Life Sciences Division

April 1998

Submitted to
Nuclear Science and Engineering

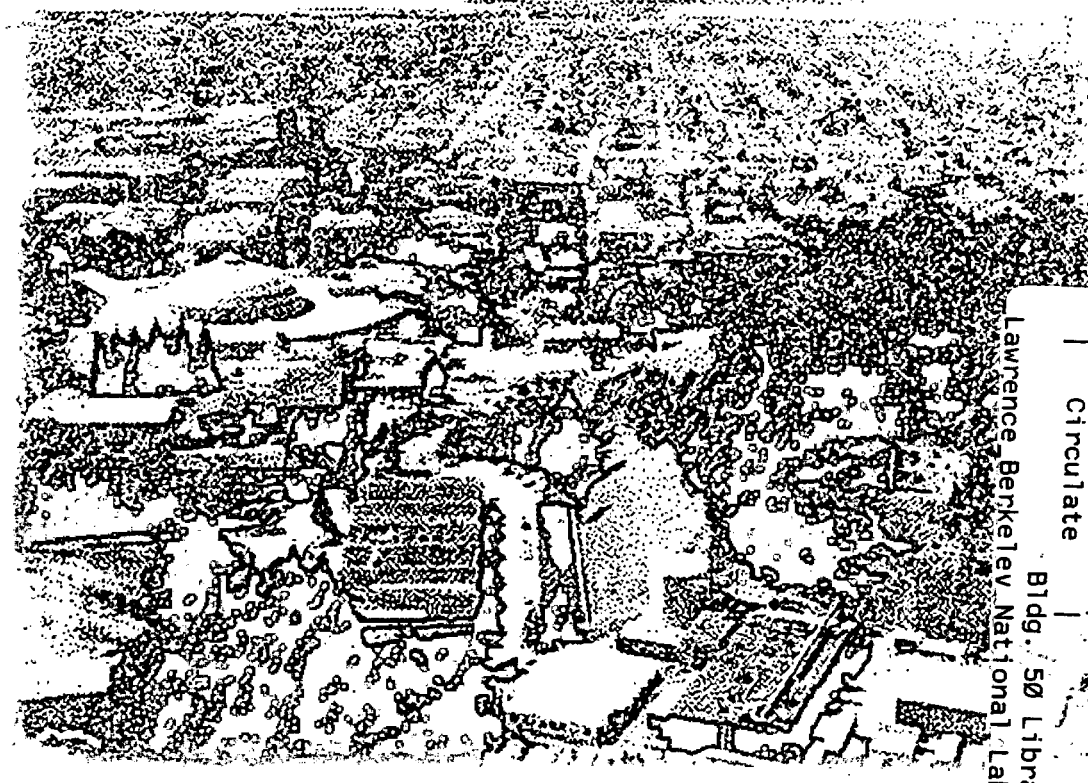

DISCLAIMER

Neutron yields from 155 MeV/nucleon C and He stopping in Al

L. Heilbronn[1], R. S. Cary[2,a], M. Cronqvist[1], F. Deák[3], K. Frankel[1], A. Galonsky[4], K. Holabird[5,b], Á. Horvath[3], Á. Kiss[3], J. Kruse[4], R. M. Ronningen[4], H. Schelin[6], Z. Seres[7], C. E. Stronach[2], J. Wang[4], P. Zecher[4,c], and C. Zeitlin[1]

(1) Life Sciences Division
Ernest Orlando Lawrence Berkeley National Laboratory
University of California
Berkeley, CA. 94720

(2) Department of Physics, Virginia State University, Petersburg, VA 23806

(3) Department of Atomic Physics, Eötvös University, Budapest 114, Hungary H-1088

(4) National Superconducting Cyclotron Laboratory and Department of Physics, Michigan State University, East Lansing, MI 48824

(5) Department of Physics, San Francisco State University, San Francisco, CA 94132

(6) CEFET-PR Department of Physics, 80230-901 Curitiba-PR, Brazil

(7) KFKI Research Institute for Particle and Nuclear Physics, Budapest 114, Hungary H-1525

April 1998

(a) Naval Surface Warfare Center, Dahlgren, VA 22448
(b) Spectra-Physics Lasers, Inc., 1335 Terra Bella Ave, Building 15, Mountain View, CA 94043
(c) Deloitte and Touche, New York, NY

This work was supported in part by the National Science Foundation under Grants PHY92-14992 and INT91-13997, by the Hungarian Government under Grant OTKA T16059, by the National Aeronautics and Space Administration under NASA Grant L14230C and NASA Grant NSG-1-1527, and through the U.S. Department of Energy under Contract No. DE-AC03-76SF00098

ABSTRACT

Neutron fluences have been measured from 155 MeV/nucleon ^{4}He and ^{12}C ions stopping in an aluminum target at laboratory angles between 10° and 160°. The resultant spectra were integrated over angle and energy above 10 MeV to produce total neutron yields. Comparison of the two systems show that approximately two times as many neutrons are produced from 155 MeV/nucleon ^{4}He stopping in Al as 155 MeV/nucleon ^{12}C stopping in Al. Using an energy-dependent geometric cross-section formula to calculate the expected number of primary nuclear interactions, it is found that the ^{12}C + Al system has slightly fewer neutrons per interaction (0.90) than does the ^{4}He + Al system (0.98), despite the fact that ^{12}C has three times as many neutrons as does ^{4}He. Energy and angular distributions for both systems are also reported. No major differences can be seen between the two systems in those distributions, except for the overall magnitude. Where possible, the ^{4}He + Al spectra are compared with previously measured spectra from 160 and 177.5 MeV/nucleon ^{4}He interactions in a variety of stopping targets. The spectra reported here are consistent with previously measured spectra. The data is applicable to problems dealing with the determination of the radiation risk to humans engaged in long-term missions in space, with the determination of the radiation environment on NASA's proposed High Speed Civil Transport, with shielding issues at high-energy heavy-ion accelerators, and with doses delivered outside tumor sites treated with high-energy, hadronic beams.

I. INTRODUCTION

In order to estimate the risk to humans exposed to a radiation field in a shielded environment, it is not enough to know the details of the primary radiation field alone. In many cases, the nature of the primary radiation field is significantly altered as it is absorbed or transported through the shielding, creating a secondary radiation field in the process. In such cases, the nature of the secondary field must also be determined. In some scenarios, the dose and dose-equivalent received from neutrons present in the secondary radiation field comprise a significant fraction of the total dose and dose-equivalent. For example, one calculation predicts that approximately 50% of the dose equivalent on a martian or lunar base made up of 50 g/cm^2 of regolith comes from neutrons [1]. Similarly, initial studies and measurements done for NASA's proposed High Speed Civil Transport indicate that neutrons make a major contribution to the dose rate at high altitudes [2]. Other scenarios where secondary neutrons are an important component of the dose equivalent are behind shielding at accelerator facilities, and in areas of the human body near tumor sites that are treated with high-energy, hadronic beams.

In the case of a thickly shielded lunar or martian base, or in the case of the upper atmosphere, neutrons are generated by interactions of primary Galactic Cosmic Rays (GCR) and solar radiation with shielding materials such as regolith or the atmosphere. GCR consist of 98% hadrons, of which 87% are protons, 12% are He, and 1% are heavier ions [3]. Most of the GCR fluence has kinetic energies between 100 MeV/nucleon and 10 GeV/nucleon, with the maximum fluence occuring between 300 and 600 MeV/nucleon, independent of particle mass. Because neutrons are produced in interactions that span a large range in projectile mass and energy, as well as

target (shielding) mass, calculational methods are the best approach to estimating the dose from neutrons in such scenarios. However, those calculational methods (Refs. 1, 4 and 5, for example) still require an extensive set of neutron production cross sections for input into the codes and thick-target neutron yields for verification of the codes' output. The data sets needed for those codes should be large enough to establish the dependency of neutron production on the projectile's mass and energy, and on the target's mass.

Although particles heavier than He make up just 1% of the GCR, a calculation has shown that approximately 16% of the neutron flux behind 50 g/cm^2 of water comes from the fragmentation of those particles (15% of the flux comes from interactions with GCR helium nuclei, with the remainder from proton-induced interactions) [5]. Calculations such as those done in Refs. 1, 4 and 5 need to make several assumptions in regard to neutron production from heavy-ion interactions because of the relative lack of pertinent experimental data. For example, in Ref. 6 the neutron production from heavy ions is generated from a simple scaling using measured proton-induced neutron cross sections and yields. Scaling heavy-ion neutron yields from proton-induced reactions will miss the component of the yield due to the breakup of the projectile, which is significant at forward angles.

In the case of atmospheric neutrons, only 25 to 30 percent of the predicted dose-equivalent comes from the measured fast neutron (1 - 10 MeV) component; the remaining 70 percent comes from unverified theoretical predictions of the neutron yield above 10 MeV. Furthermore, it is believed that current atmospheric environmental models may be significantly underpredicting the yield of high energy (greater than 10 MeV) neutrons [2, 7].

The neutron yields from 155 MeV/nucleon ^{12}C and ^{4}He stopping in an Al target have been measured in order to provide some information on the nature of the high-energy neutron yield, as well as to investigate the dependence of the neutron yield on projectile mass. Neutron yields were measured at laboratory angles between 10 and 160 degrees, and for neutron energies 10 MeV and above. In addition to the neutron spectra at each angle, angular distributions and energy distributions from each system are presented, as well as total neutron yields.

II. EXPERIMENTAL DETAILS

The data presented here come from a neutron time-of-flight experiment that was performed at Michigan State University's National Superconducting Cyclotron Laboratory. Beams of fully-stripped 155 MeV/nucleon ^{12}C and ^{4}He were delivered on target in one to three-ns wide bursts. In each case the period of the beam burst was 41.6 ns. Beam spot size at the target was typically 0.5 cm in diameter. For normalization purposes, the number of beam particles incident on the target was calculated from the total amount of charge collected in the Al target, as read by a current integrator. The target was a 13.34-cm long, 1.78-cm diameter cylinder of Al, with a 5.08-cm long, 1.59-cm diameter bore cut into the entrance of the target (the beam's axis coincided with the target's cylindrical axis). The target bore minimized the loss of back-scattered delta-electrons, which improved the charge-collection properties of the target. The target was suspended inside a

91.44-cm diameter steel scattering chamber with 3.2-mm thick walls. Typical pressure inside the scattering chamber and beam line was 10^{-6} torr.

Neutron detectors were placed outside the scattering chamber at laboratory angles between 10° and 160°. Each neutron detector consisted of liquid scintillator (BC-501 or NE-213) encased in a cylindrical cell constructed of either glass or aluminum. The detector cells were typically 12.7 cm in diameter and either 7.62 cm or 5.08 cm long. Arrays of 7 neutron detectors bundled together were placed at 10°, 30°, 45°, and 60°. An array of 3 detectors was placed at 90°, and individual detectors were placed at 125°, 160°, −30°, −45°, and −60° (a minus sign indicates the detectors were placed on the right-hand side of the beam). Solid plastic scintillators 6.35-mm thick and 12.7 cm in diameter, referred to as "veto detectors", were placed between the neutron detectors and the target in order to register any events in the neutron detectors created by charged particles energetic enough to traverse the materials lying between the target and neutron detector. Cylindrical bars of brass or steel were periodically placed between the target and neutron detectors in order to stop neutrons coming directly from the target. These allowed only background neutrons, such as room-scattered neutrons, to hit the neutron detectors. Figure 1 shows an overhead view of the experimental setup. Tables I, II and III contain information in regard to the neutron detectors, veto detectors, and shadow bars.

Data were recorded on an event-by-event basis. A master trigger was generated by any event in a neutron detector which was above the detector's constant fraction discriminator's (CFD) threshold. CFD thresholds were typically set to one to three times the ^{60}Co Compton edge. For each event the following information was recorded: (1) the number of the neutron detector in which the event took place, (2) the total charge collected in the anode pulse from the neutron detector, (3) the charge collected in the tail of the anode pulse from the detector, (4) the relative time between the event in the neutron detector and a RF signal from the cyclotron, (5) a flag indicating whether or not the companion veto detector also registered an event, and (6) the total amount of charge collected in the anode signal from the veto detector. In addition, information regarding the live time, total charge collected in the target, total number of events in each detector, and pre-scale factors was recorded from each run.

III. DATA ANALYSIS

A. Neutron energy determination

Neutron energies were determined by measuring the time of flight between a signal from cyclotron RF and a timing signal generated from the anode of the neutron detector. The RF signals were prescaled by a factor of 4 so that groups of 4 sequential beam bursts were timed against a single RF signal. Figure 2 shows the TDC (time-to-digital convertor) spectrum for neutron detector #33 (160°). Time increases from right to left. Gamma-ray events are shown with the solid histogram and neutron events are shown with the dotted histogram. The peaks labeled A, B, C, and D

are from prompt gamma rays created by separate beam bursts striking the target. The widths (FWHM) of those peaks have an average value of approximately 1 ns, and that value is used as the overall timing resolution in the experiment, which in turn is used to set the minimum bin width in the energy spectra generated from the TDC spectra. Neutron events were separated offline from gamma-ray events using the technique described by Heltsley, et al. [8], which takes advantage of the different pulse shapes created by neutron-induced and gamma-ray-induced events in the liquid-scintillator cell. By plotting the amount of charge in the tail of the pulse versus the amount of charge in the entire pulse, two distinct lines, one each for neutron and gamma-ray events, could be seen and used to separate the two classes of events.

The TDC spectra were calibrated by measuring the number of channels between prompt gamma-ray peaks and using the known period (41.6 ns) of the beam bursts. The time of flight for a neutron event is calculated using the measured time difference between it and the nearest, prior prompt gamma-ray peak, and adding to that the time of flight for a gamma ray to go from the target to the neutron detector. For example, a neutron event in channel n of Fig. 2 has the corresponding time of flight:

$$TOF_n = [k(CHAN_b - CHAN_n)] + TOF_g, \tag{1}$$

where $CHAN_b$ is the TDC channel number of the prompt gamma-ray peak labeled B in Fig. 2, $CHAN_n$ is the TDC channel number of "n", k is the TDC channel-to-time conversion factor, and TOF_g is the time of flight for a prompt gamma ray to go from the target to the neutron detector. Using the flight path from target to detector, the neutron's velocity is calculated from its time of flight. The neutron's energy is then calculated from its velocity using relativistic kinematics.

B. Background subtraction

In addition to the neutrons that go directly from the target to the neutron detector, the neutron detectors also register background events resulting from room-scattered neutrons that go indirectly from the target into the detector. Shadow bars (see experimental section above) were placed between the target and the neutron detectors at various times during the experiment which allowed the measurement of only the background neutrons. Runs without the shadow bars measured both the direct and background neutrons. By subtracting the shadow-bar raw data from the non-shadow-bar raw data (after normalizing the runs to each other for run time, computer live time, etc..) the direct neutron spectra were separated from the background spectra.

C. Wraparound neutrons and QDC calibration

As can be seen in Fig. 2, an event in the TDC spectrum may come from any one burst in a set of sequential beam bursts. For example, an event that winds up in the channel labeled n in Fig. 2 may be a relatively high-energy neutron that came from the beam burst that produced

the prompt gamma ray peak B, or it may be a much lower energy neutron that came from the beam burst corresponding to peak A. Such a low-energy neutron from a preceding beam burst is referred to as a wraparound neutron. Equation 1 is not valid for wraparound neutrons, and those neutrons must be removed from the raw data before energy spectra are produced.

The first step in eliminating wraparound neutrons is to determine at what energy neutrons from a preceding beam burst start to wrap around with neutrons from the beam burst that is used in Eqn. 1. That value was found by computing the energy of a neutron (referred to as the wraparound energy) from the preceding burst that winds up in the prompt-gamma peak location of the beam burst used in Eqn. 1. For example, in Fig. 2, the energy of a neutron coming from beam burst A that has the same TDC value as the prompt-gamma ray peak labeled B is 9.5 MeV. Thus, all neutrons from beam burst A with energies 9.5 MeV and lower will wrap around with neutrons coming from beam burst B.

The next step is to apply a cut to the data that eliminates all neutrons with energies up to and including the wraparound energy. Although there is no direct measure of the neutron's energy, the QDC (charge-to-digital convertor) measures the amount of charge produced by light that is created in the scintillator via neutron interactions with charged particles in the liquid. A neutron of a given energy can produce any amount of light up to a maximum that is produced when the neutron has a direct collision with a proton, transferring all of its momentum to the proton. By making a cut on QDC values that corresponds to the maximum amount of light produced by a neutron with the wraparound energy, all wraparound neutrons can be eliminated, leaving only neutrons with energies greater than the wraparound energy. To continue the example in Fig. 2, finding the QDC value that corresponds to the light produced by a 9.5-MeV proton, and by eliminating all events that have that QDC value or lower, wraparound neutrons are eliminated from the data.

In order to correctly apply a QDC threshold to the data, the QDC spectra were converted to units of recoil-proton energy (equivalent to neutron energy for direct collisions). Two different methods were used to convert QDC values to recoil-proton energy. The first method takes advantage of the fact that some protons created in the target have sufficient energy to reach the detector. Such events will have a positive veto signal. A scatter plot of QDC value versus TDC value for these events shows a line that corresponds to high-energy protons. In some cases, lines corresponding to deuterons and tritons can also be observed. By choosing points along the proton line, one can determine the direct correspondence between QDC value and time of flight of the proton. Furthermore, by knowing the thicknesses and positions of materials the proton went through to get to the neutron detector, and by using proton energy loss tables [9], the energy of a proton as it enters the neutron detector can be calculated as a function of its time of flight. Thus, a direct relationship between proton energy and QDC response is determined. A plot of QDC value versus proton energy for detector #9 (30°) is shown in Fig. 3. The values obtained using this method are shown with the diamond-shaped symbols. At 30° the wraparound energy is 29.5 MeV, and the corresponding QDC threshold value then used to eliminate wraparound neutrons can be directly read off that plot.

The second method used to calibrate the QDC spectra involved producing a plot of the detector's QDC value versus TDC value, but gated on neutron events only. In such plots a clear demarcation

is observed between QDC values where a neutron can produce light via recoil and QDC values where it is kinematically impossible for a neutron of a given energy to produce such a value. The point of demarcation at a particular TDC value corresponds to the maximum amount of light produced by a neutron of the appropriate energy. The QDC value at the demarcation point is assumed to be equivalent to the amount of light produced by a proton that received the maximum amount of momentum transfer from the incoming neutron. Thus, by determining the neutron's energy from its TDC value, and by assuming the QDC value at the demarcation point is produced by a proton of the same energy, a second, independent set of values of QDC versus proton energy is generated. The values obtained using this method for detector #9 are shown in Fig. 3 with the X-shaped symbols.

The agreement between the two methods is good, in general. The two methods agreed with each other to no worse than $\pm$ 50 channels, and on average were within $\pm$ 25 channels. An uncertainty of $\pm$ 25 channels on the QDC threshold led to an uncertainty of $\pm$ 10 to 15 percent on the yields in the double differential spectra.

D. Efficiency, attenuation, and normalization factors

After the neutron spectra were converted from units of TDC channel number to units of energy, the spectra were corrected for neutron detection efficiency using the code developed by Cecil et al. [10]. Figure 4 shows the neutron detection efficiency for detector #9 for a QDC threshold equivalent to 29.5 MeV in neutron energy. For the sake of comparison, the detection efficiency for detector #9 using a 15.5-MeV threshold is also shown.

The spectra were also corrected for the loss of neutron flux due to scattering by materials between the target and the detector. To accomplish this, a Monte Carlo code was written that included all relevant neutron elastic and inelastic scattering cross sections. Also included was all the relevant geometric information, such as detector dimensions, thicknesses of materials between the target and detector, and positions of those materials in the laboratory. The code kept track of the number of neutrons that did and did not reach the neutron detector. Figure 5 shows the result of the calculation done for detector #9, showing the fraction of neutrons that reach the detector as a function of neutron energy. The spectrum of actual events in detector #9 is corrected by dividing by the appropriate fraction given in Fig. 5. The results of the code used here were compared with the results of a code written by Remington [11]. The two agreed with each other to within 10%, and that value was taken as the systematic error on the flux-attenuation correction.

Neutron spectra were also corrected for computer dead time and for pre-scale factors. The spectra were normalized to the number of incident beam particles, which were counted by using the Al target as a Faraday cup and connecting the target to a current integrator.

IV. EXPERIMENTAL RESULTS

The spectra reported here include neutrons produced in the target by interactions of the primary ion, interactions by all secondary particles, and neutron interactions in the target. No corrections were made to the fluences due to neutron transport through the target. All reported yields, then, pertain to the fluence as it leaves the target.

Except where noted, the uncertainties shown in the figures and tables are statistical. The systematic uncertainties mainly affect the overall scale of the spectra, and include contributions from uncertainties in the efficiency calculation, flux-attenuation calculation (10%, see section III.D), QDC wraparound-threshold determination (10-15%, see section III.C), solid angle determination, and number of incident ions.

The systematic uncertainty in the efficiency calculation was estimated by comparing the results of the calculation used here with another efficiency calculation [12], assuming a precisely defined threshold. The two calculations disagreed by at most 10%, and that value is taken as the uncertainty in the efficiency calculation.

The systematic uncertainty in the solid angle stems mainly from the uncertainty in the location of neutron production within the stopping target and the difference in the solid angle at the front face of the detector and at the back face of the detector. This uncertainty is estimated by calculating the solid angles at the production point in the target nearest to the front face of the detector and at the production point farthest from the back face of the detector, and then taking half of the difference between the two values. Because the range of the He beam is longer than the C beam, the uncertainty is greater for the He data set than it is for the C data set. The uncertainty is greatest at 160°, where it is 7.4% for the He + Al data, and 5.0% for the C + Al data. The uncertainties for all detectors are listed in Table I.

The systematic uncertainty in the number of incident ions is primarily due to losses of delta electrons and secondary protons from the target. Using the data from the veto detectors to estimate the number of protons that escape the target, the systematic uncertainty in the number of ions is taken to be less than five percent.

Summing the individual contributions to the systematic uncertainty in quadrature yields an overall systematic uncertainty of 20-25%. As a check on the overall systematic uncertainty, the yields from detectors in the same detector bundle were compared to each other. Because the data from each detector require a separate efficiency calculation, flux-attenuation calculation, solid-angle calculation, and QDC wraparound-threshold determination, that comparison will be sensitive to the contributions to the systematic uncertainty mentioned above, except for the uncertainty in the number of beam ions. The variance of the yields within the same bundle was on the order of 20%, which is in agreement with the estimated systematic uncertainty.

A. Double-differential yield spectra

Figure 6 shows the double-differential spectra (in units of number of neutrons per MeV per millisteradian per incoming ion) for the ^{12}C + Al system at 10°, 45°, 90°, 160° (left plot), and 30°, 60°, 125° (right plot). The contribution of neutrons from the breakup of the projectile can

be seen at 10° in the form of the broad peak that starts around 50 MeV and extends to energies above the incident energy per nucleon. The broad peak of projectile-like neutrons is in contrast with the relatively narrow peak seen in thin-target cross section measurements (see, for example, Ref. 13) because the projectile interacts with the target at all energies up to the incident energy of 155 MeV/nucleon. At angles of 45° and greater, the spectra show an exponential fall-off with increasing energy, which is indicative of equilibrium and pre-equilibrium neutron emission [14].

Figure 7 shows the double-differential spectra for the ^{4}He + Al system in the same format as in Fig. 6. The features seen in the ^{12}C + Al system can also be seen in the ^{4}He + Al system. Wider energy-binning was used in the ^{4}He + Al data because the ^{4}He beam pulse was wider than the ^{12}C beam pulse (3-ns wide versus 1-ns wide, respectively), which led to a larger value of the timing resolution.

As a check on overall normalization, the 45° and 90° ^{4}He + Al data can be compared with a similar measurement done with 160 MeV/nucleon ^{4}He stopping in a Pb target [15]. Table IV shows the comparison between the two systems in yields in units of number per MeV per steradian per 10^6 incoming ions. The uncertainties reported in Table IV are the statistical uncertainties. The main difference between the two systems is the mass of the target. However, the authors of Ref. 15 found that for 177.5 MeV/nucleon ^{4}He stopping in targets of C, water, Fe, and Pb, the total yield was independent of target mass. An analysis of the double-differential spectra from those systems shows that the yields at a particular energy and angle vary at most ±20% with target mass. A comparison between the 155 MeV/nucleon ^{4}He + Al and 160 MeV/nucleon ^{4}He + Pb data sets in Table IV shows a similar variation. This indicates that the spectra reported here are consistent with the only other reported stopping-target data for this ion species and energy range.

B. Energy and angular distributions

Figure 8 shows the energy distributions for the ^{12}C + Al system (shown with the X-shaped symbol) and ^{4}He + Al system (shown with the diamond-shaped symbol). These spectra were generated by integrating the seven double-differential spectra (10°, 30°, 45°, 60°, 90°, 125°, and 160°) from 0° to 180°. The two systems are very similar in shape, which can be characterized as an exponential fall-off with increasing energy, along with a small "hump" or "shoulder" between 50 and 200 MeV. The shoulder is likely due to the contribution from the decay of the projectile remnant. The main difference between the two systems is that the magnitude of the ^{12}C + Al spectrum is approximately a factor of two less than the ^{4}He + Al spectrum.

Figure 9 shows the angular distributions from the ^{12}C + Al (X-shaped symbols) and the ^{4}He + Al (diamond-shaped symbols) systems. These distributions were obtained by integrating the double-differential spectra over energy above 10 MeV. Both spectra show the same dependence of yield on angle, with the only major difference between the two being their relative magnitudes.

The solid and dashed lines in Fig. 9 show a fit to the data based on a superposition of two exponentials:

$$y = a_1 \exp(-a_2\theta) + a_3 \exp(-a_4\theta), \tag{2}$$

where a_1, a_2, a_3, and a_4 are fit parameters and y is the number of neutrons per msr. Table V shows the fit parameters for both systems, using units of degrees for θ in Eqn. 2. Within uncertainties, the slope parameters a_2 and a_4 are the same for both systems.

C. Total yields

Table VI shows the total yield for each system, obtained by integrating the spectra in Fig. 8 over energy (above 10 MeV) and over angle from 0° to 180°. The total yields are expressed in units of number of neutrons per incident ion. Also shown in Table VI are the estimated fractions of beam ions which undergo a nuclear interaction in the stopping target, as calculated using an energy-dependent geometric cross-section equation [16]. The fourth column in Table VI, which shows the number of neutrons per interaction as calculated by dividing the number in the second column by the number in the third column, shows that somewhat fewer neutrons-per-interaction are emitted from the ^{12}C + Al system than from the ^{4}He + Al system. In both systems, the total yield is close to 1 neutron above 10 MeV per interaction. The fact that the number of neutrons per interaction is almost the same between the two systems indicates that the total yields scale, to first order, with the expected fraction of nuclear interactions per beam ion.

The fact that the total number of neutrons per interaction is nearly equal for both systems despite the fact that ^{12}C has 3 times the number of neutrons as does ^{4}He may be due to : (1) The total number of neutrons in the ^{12}C + Al system (20) is close to the total number of neutrons in the ^{4}He + Al system (16). This would suggest that the total yields are dominated by interactions that involve the breakup of the entire system of projectile plus target. However, much of the yield at forward angles and at high neutron energies comes from the breakup of the projectile, so this reason alone cannot explain why the total yields per interaction are independent of projectile mass. (2) Nuclear structure effects, such as alpha or deuteron clustering within the nucleus, may strongly bind neutrons with other nucleons and suppress breakup channels which emit free neutrons. The breakup of the ^{12}C nucleus, which has a filled $1p_{3/2}$ subshell, may be affected at this energy by structure effects; this could be tested by repeating this experiment with a projectile that has neutrons not as strongly bound, such as ^{14}N, to compare the total yields from that system to those reported here.

The total yield from the 155 MeV/nucleon ^{4}He + Al system is 0.35 neutrons per incoming ion for neutrons with energies greater than 10 MeV. As noted previously, the authors of Ref. 15 found that the total yields above 10 MeV from the 177.5 MeV/nucleon ^{4}He systems were about 0.5 neutrons per incoming ion, independent of target mass. They also noted that the yields from the 160 MeV/nucleon ^{4}He + Pb system were about 20% less than the yields from the 177.5 MeV/nucleon ^{4}He systems, thus a total neutron yield of approximately 0.4 neutrons above 10 MeV per ion is estimated for the 160 MeV/nucleon system. Because the total yield dropped from 0.5 neutrons per ion at 177.5 MeV/nucleon to an estimated 0.4 neutrons per ion at 160 MeV/nucleon, it is presumed that the estimated yield will drop further as the beam energy goes from 160 to 155 MeV/nucleon. Our value of 0.35 neutrons per ion for the 155 MeV/nucleon ^{4}He + Al system is consistent with that estimate, within the systematic uncertainty of ± 20%.

Figure 10 shows a plot of the total yields for both systems above a given neutron energy. ^{4}He yields are shown with the diamond-shaped symbols, and ^{12}C yields are shown with the X-shaped symbols. The ratio of the yields between the two systems remains the same (2:1 for He:C) no matter what neutron-energy cutoff is used. The dependence of the total yield on neutron-energy cutoffs between 10 and 100 MeV shows a slightly different behavior than what was observed in Ref. 15, which found a power-law relationship between yield and cutoff energy for cutoff energies between 1 and 50 MeV. For the data here, the best fits are obtained by using an exponential of the form

$$Y(> E) = a \times exp^{-(bE)},$$

where a = 0.20 ± 0.03, b = 0.017 ± 0.003 for the ^{12}C + Al system, and a = 0.40 ± 0.08, b = 0.017 ± 0.004 for the ^{4}He + Al system (both fits shown with a solid line in Fig. 10). However, it should be noted that if the points above 50 MeV in Fig. 10 are excluded, the remaining data are fitted reasonably well with a power-law relationship of the form

$$Y(> E) = aE^{-b},$$

where a = 0.52 ± 0.05, b = 0.44 ± 0.03 for the ^{12}C + Al system and a = 1.00 ± 0.13, b = 0.45 ± 0.04 for the ^{4}He + Al system (fits shown with the dashed lines in Fig. 10).

VI. CONCLUSIONS

Neutron yields from 155 MeV/nucleon ^{12}C and 155 Mev/nucleon ^{4}He stopping in an aluminum target were measured for the purpose of providing data relevant to shielding issues of concern for deep-space missions, high-altitude flights, and radiation therapy using heavy-ion beams. Double-differential spectra at 10°, 30°, 45°, 60°, 90°, 125°, and 160° were measured for both systems. Comparisons of the 45° and 90° ^{4}He + Al spectra measured here with previously measured 160 MeV/nucleon ^{4}He + Pb spectra at the same angles show the two measurements are consistent with each other and are consistent with neutron yield being independent of target mass. Angular and energy distributions have been extracted from the double-differential spectra, and both systems exhibit the same behavior, with the only difference being the magnitudes of each. Total neutron yields for neutron energies above 10 MeV were also extracted. Despite the fact that ^{12}C has three times the number of neutrons as does ^{4}He, the total yield per nuclear interaction is slightly less for the ^{12}C + Al system than it is for the ^{4}He + Al system, with both systems yielding on the order of one neutron per interaction; this result may be an indication that nuclear structure effects within these two ions are favoring other breakup channels over neutron decay channels for neutron energies above 10 MeV.

ACKNOWLEDGMENTS

The authors wish to thank the staff of the National Superconducting Cyclotron Laboratory for their help and support during all stages of the experiment. We also thank Danielle Green and Xochitl Leon for their assistance with the data analysis.

This work was supported in part by the National Science Foundation under Grants PHY92-14992 and INT91-13997, by the Hungarian Government under Grant OTKA T16059, and by the National Aeronautics and Space Administration under NASA Grant L14230C and NASA Grant NSG-1-1527.

Present Address:

(a) - Naval Surface Warfare Center, Dahlgren, VA 22448

(b) - Spectra-Physics Lasers, Inc., 1335 Terra Bella Ave, Building 15, Mountain View, CA 94043

(c) - Deloitte and Touche, New York, NY

REFERENCES

1. L. C. Simonsen and J. E. Nealy, NASA Technical Paper 3079 (1991).

2. NCRP Commentary No. 12 "Radiation Exposure and High-Altitude Flight", National Council on Radiation Protection and Measurements, NCRP Publications, Bethesda, Md. (1995).

3. J. A. Simpson, "Introduction to the galactic cosmic radiation", page 1 in *Composition and Origin of Cosmic Rays*, Reidel Publishing, Dorcht, Netherlands (1983).

4. L. C. Simonsen, J. E. Nealy, L. W. Townsend, and J. W. Wilson, NASA Technical Paper 2979 (1990).

5. F. A. Cucinotta, NASA Technical Paper 3354 (1993).

6. T. Foelsche, R. B. Mendell, J. W. Wilson, and R. R. Adams, NASA TN D-1383 (1974).

7. J. W. Wilson, J. E. Nealy, F. A. Cucinotta, J. Shinn, F. Hajnal, M. Reginatto, and P. Goldhagen, NASA Technical Paper 3524 (National Technical Information Service, Springfield, VA.) (1995).

8. J. H. Heltsley, L. Brandon, A. Galonsky, L. Heilbronn, B. A. Remington, S. Langer, A. VanderMolen and J. Yurkon, Nucl. Instr. and Meth **A263**, 441-445 (1988).

9. J. F. Janni, Atomic Data and Nuclear Data Tables **27** numbers 2-5 (1982).

10. R. A. Cecil, B. D. Anderson, and R. Madey, Nucl. Instrum. Methods **161**, 439 (1979).

11. B. A. Remington, Ph.D. Thesis, Michigan State University (1986).

12. R. J. Kurz, University of California Radiation Lab Internal Report No. URCL-11339 (1964)

13. A. R. Baldwin, R. Madey, W.-M. Zhang, B. D. Anderson, D. Keane, J. Varga, J. W. Watson, G. D. Westfall, K. Frankel, and C. Gale, Phys. Rev. C **46**, 258 (1992).

14. T. Nakamura, Nucl. Instr. and Meth. **A240**, 207 (1985).

15. R. A. Cecil, B. D. Anderson, A. R. Baldwin, R. Madey, A. Galonsky, P. Miller, L. Young, and F. M. Waterman, Phys. Rev. C **21**, 2471 (1980).

16. L. W. Townsend and J. W. Wilson, Phys. Rev. C **37**, 892 (1988).

TABLE I. Position, flight path, and solid angle subtended by the neutron detectors used in the experiment. The flight paths are measured from the target to the center of the detector. The two numbers in the parentheses are the percent systematic-uncertainties in the solid angle for the ^{12}C run and ^{4}He run, respectively (see text).

Detector number	angle (deg)	flight path (cm)	solid angle (msr)
1	10	404.1	0.775 (2.6, 3.7)
2	10	405.3	0.720 (2.5, 3.7)
3	10	404.9	0.697 (2.6, 3.7)
4	10	404.9	0.773 (2.6, 3.8)
5	10	404.9	0.773 (2.6, 3.8)
6	10	406.2	0.768 (2.0, 3.1)
7	10	405.2	0.772 (2.6, 3.8)
8	30	404.1	0.776 (2.4, 3.6)
9	30	405.9	0.769 (1.8, 2.9)
10	30	409.9	0.741 (2.3, 3.4)
11	30	405.2	0.732 (2.5, 3.6)
12	30	406.2	0.768 (1.8, 2.9)
13	30	405.1	0.726 (2.3, 3.4)
14	30	405.9	0.741 (2.3, 3.4)
15	45	403.8	0.787 (2.3, 3.2)
16	45	406.2	0.768 (1.7, 2.6)
17	45	404.9	0.773 (2.3, 3.2)
18	45	405.1	0.729 (2.3, 3.2)
19	45	404.9	0.773 (2.3, 3.2)
20	45	405.1	0.732 (2.3, 3.2)
21	45	405.0	0.733 (2.2, 3.2)
22	60	353.8	1.025 (2.4, 3.1)
23	60	354.3	0.772 (1.9, 2.7)
24	60	354.1	1.023 (2.4, 3.1)
25	60	354.1	1.023 (2.4, 3.1)
26	60	354.1	1.023 (2.4, 3.1)
27	60	354.1	1.023 (2.4, 3.1)
28	60	354.1	1.023 (2.4, 3.1)
29	90	243.1	2.144 (2.1, 2.1)
30	90	242.1	2.040 (3.1, 3.1)
31	90	241.8	1.955 (3.2, 3.2)
32	125	232.9	2.335 (3.9, 5.1)
33	160	202.6	7.901 (5.0, 7.4)
35	-30	203.8	3.088 (4.7, 6.9)
36	-45	204.9	2.849 (4.6, 6.4)
37	-60	204.9	3.017 (4.3, 5.6)

TABLE II. Position and flight path for the veto detectors used in the experiment. The flight paths are measured from the target to the center of the detector.

Veto detector angle (deg)	flight path (cm)
10	116.8
30	125.7
45	125.1
60	100.3
90	106.0
125	221.0
160	154.8
-30	194.3
-45	190.5
-60	193.0

TABLE III. Position, length, diameter, and flight path for the shadow bars used in the experiment. The flight paths are measured from the target to the center of the shadow bar.

angle (deg)	length (cm)	diameter (cm)	flight path (cm)
10	36.8	10.16	81.9
30	40.6	8.89	66.0
45	29.8	8.89	60.6
60	30.2	10.16	60.8
90	30.5	10.16	61.0
125	29.5	7.62	60.5
160	29.5	7.62	60.5
-30	29.2	7.62	60.3
-45	29.5	7.62	60.5
-60	29.5	7.62	78.9

TABLE IV - Comparison of 45° and 90° ^{4}He + Al data with 160 MeV/nucleon ^{4}He + Pb data from Ref. 15. Energies are in units of MeV, and yields are in units of number per MeV per steradian per 10^6 incoming ions.

155 MeV/nucleon ^{4}He + Al		160 MeV/nucleon ^{4}He + Pb	
45 degrees energy	yield	45 degrees energy	yield
17.4	886 ± 37	16.3	1080 ± 65
22.4	720 ± 36	20.9	857 ± 47
29.8	671 ± 23	27.3	655 ± 36
42.1	520 ± 15	37.1	505 ± 25
90 degrees energy	yield	90 degrees energy	yield
12.4	515 ± 46	13.2	581 ± 35
17.4	314 ± 24	17.8	381 ± 23
22.4	245 ± 17	23.8	257 ± 15
27.4	179 ± 15		
		31.8	141 ± 8
34.8	128 ± 9		
		42.3	94.4 ± 6.6
49.4	61 ± 4		
		56.2	46.7 ± 4.2
78.3	17 ± 2	81.6	19 ± 3

TABLE V - Fit parameters from Equation (2) for both systems. θ in Equation 2 is in units of degrees.

	^{12}C + Al	^{4}He + Al
a_1	0.000050 ± 0.000008	0.000060 ± 0.000005
a_2	0.0232 ± 0.0012	0.021 ± 0.003
a_3	0.00020 ± 0.00003	0.00043 ± 0.00009
a_4	0.074 ± 0.006	0.066 ± 0.008

TABLE VI - Total yields for the the two systems in units of number per incoming ion. The third column shows the fraction of beam particles expected to undergo a nuclear interaction in the target. The fourth column shows the number of neutrons per nuclear interaction.

system	yield	interaction fraction	number per interaction
$^{12}C + Al$	0.179 ± 0.005	0.199	0.90 ± 0.03
$^{4}He + Al$	0.348 ± 0.013	0.354	0.98 ± 0.04

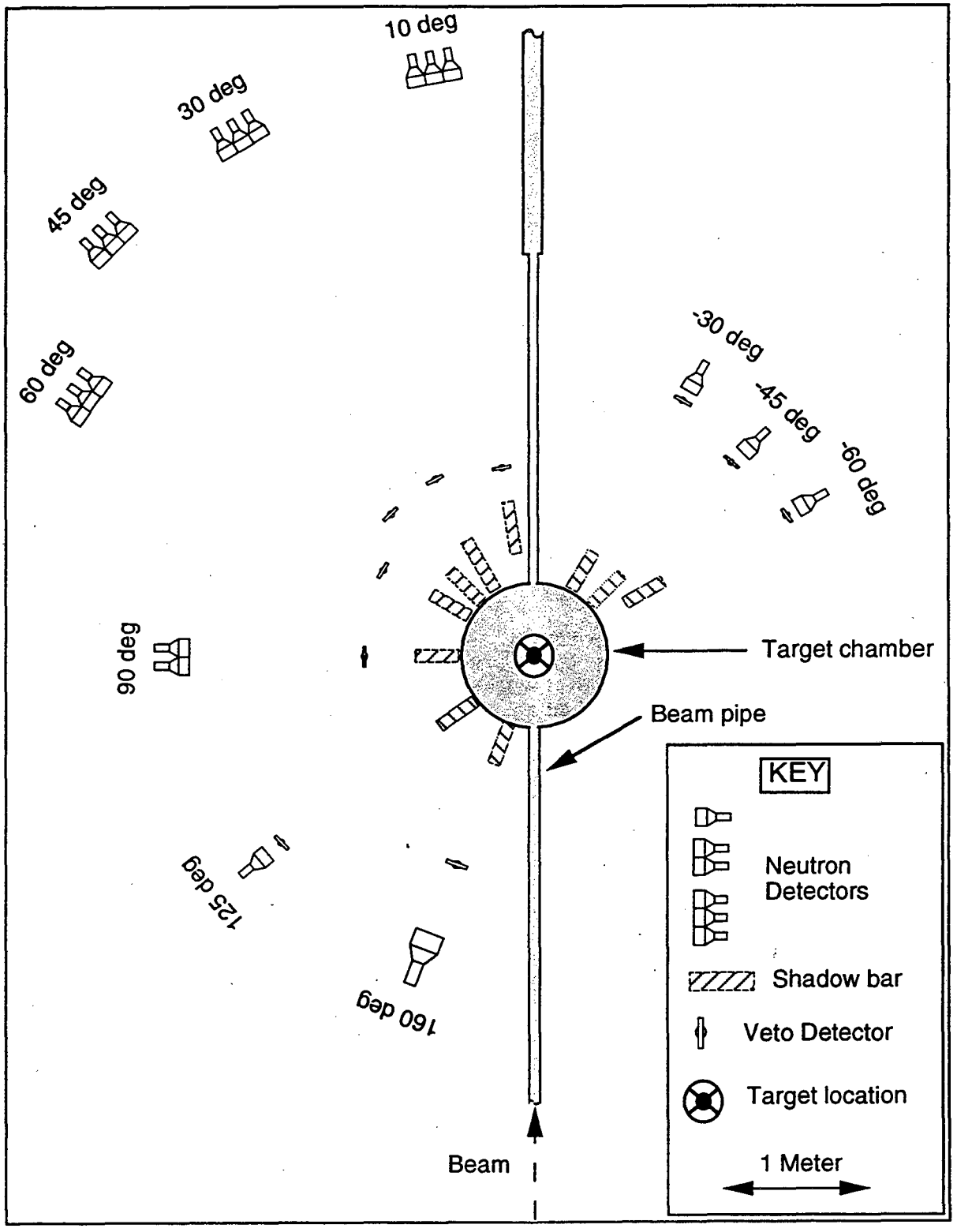

Fig. 1 - Overhead view of the experimental setup in the N4 vault at the NSCL.

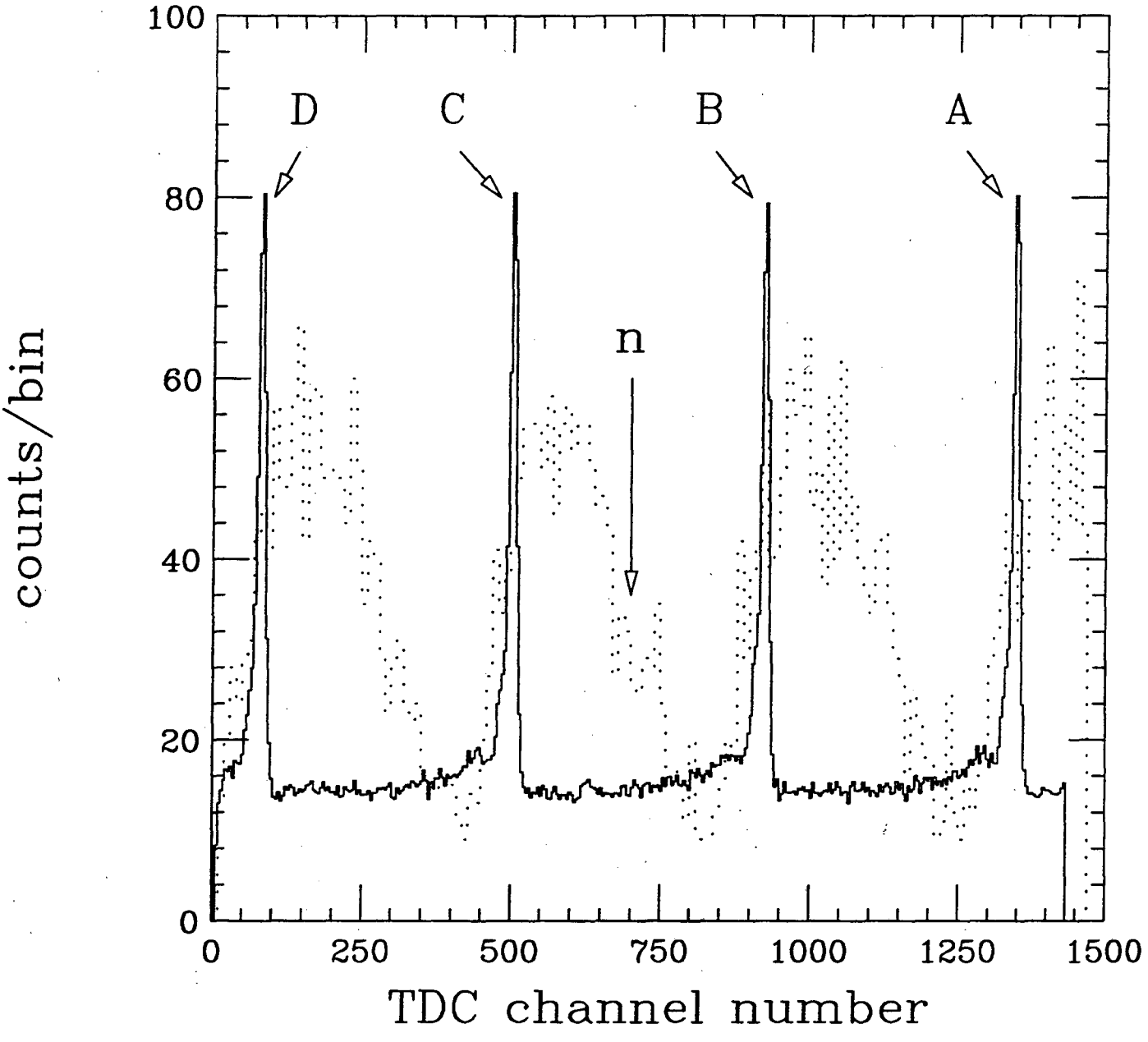

Fig. 2 - Time-to-digital convertor (TDC) spectrum for detector #33. Time increases from right to left. Gamma-ray events are indicated with the solid histogram, and neutron events are indicated with the dotted histogram. The peaks labeled A, B, C, and D are due to prompt gamma rays created by successive beam bursts striking the target.

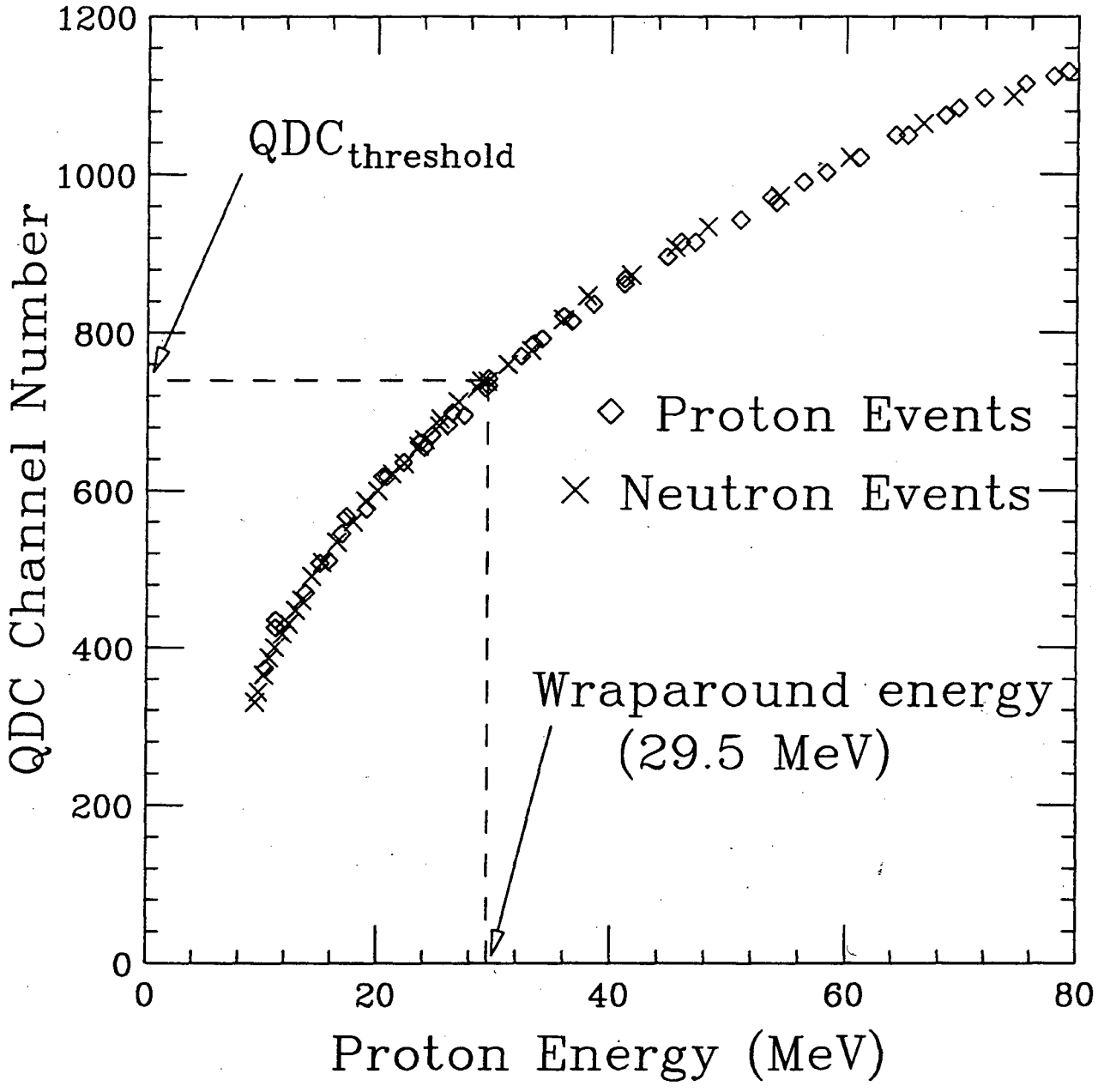

Fig. 3 - Plot of QDC channel number versus recoil proton energy for detector #9. The two different symbols represent two different methods used for obtaining the recoil proton energy, as described in the text.

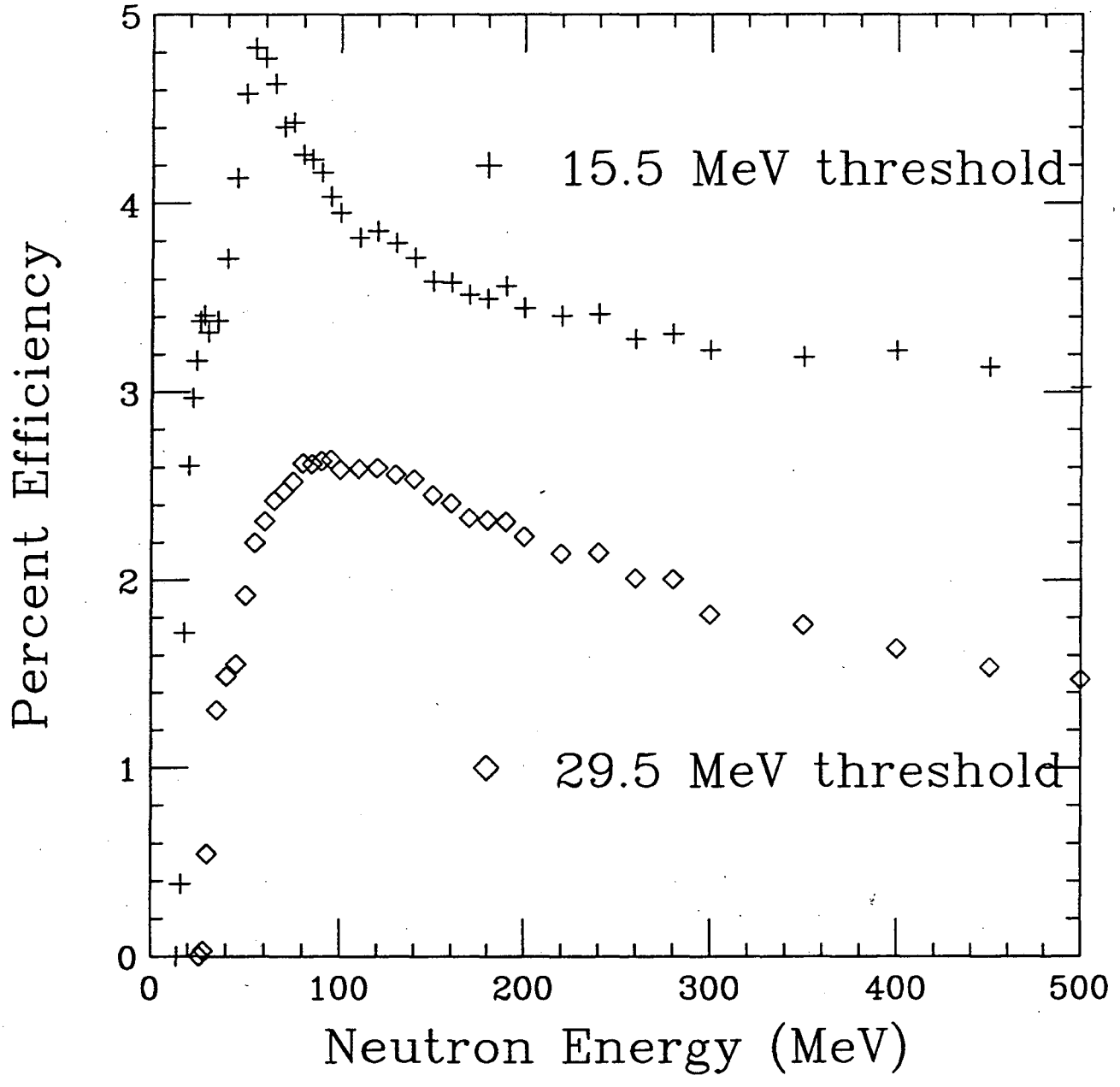

Fig. 4 - Neutron detection efficiency as a function of neutron energy for detector #9, using the indicated thresholds. The efficiency was calculated using the code developed by Cecil et al. [10].

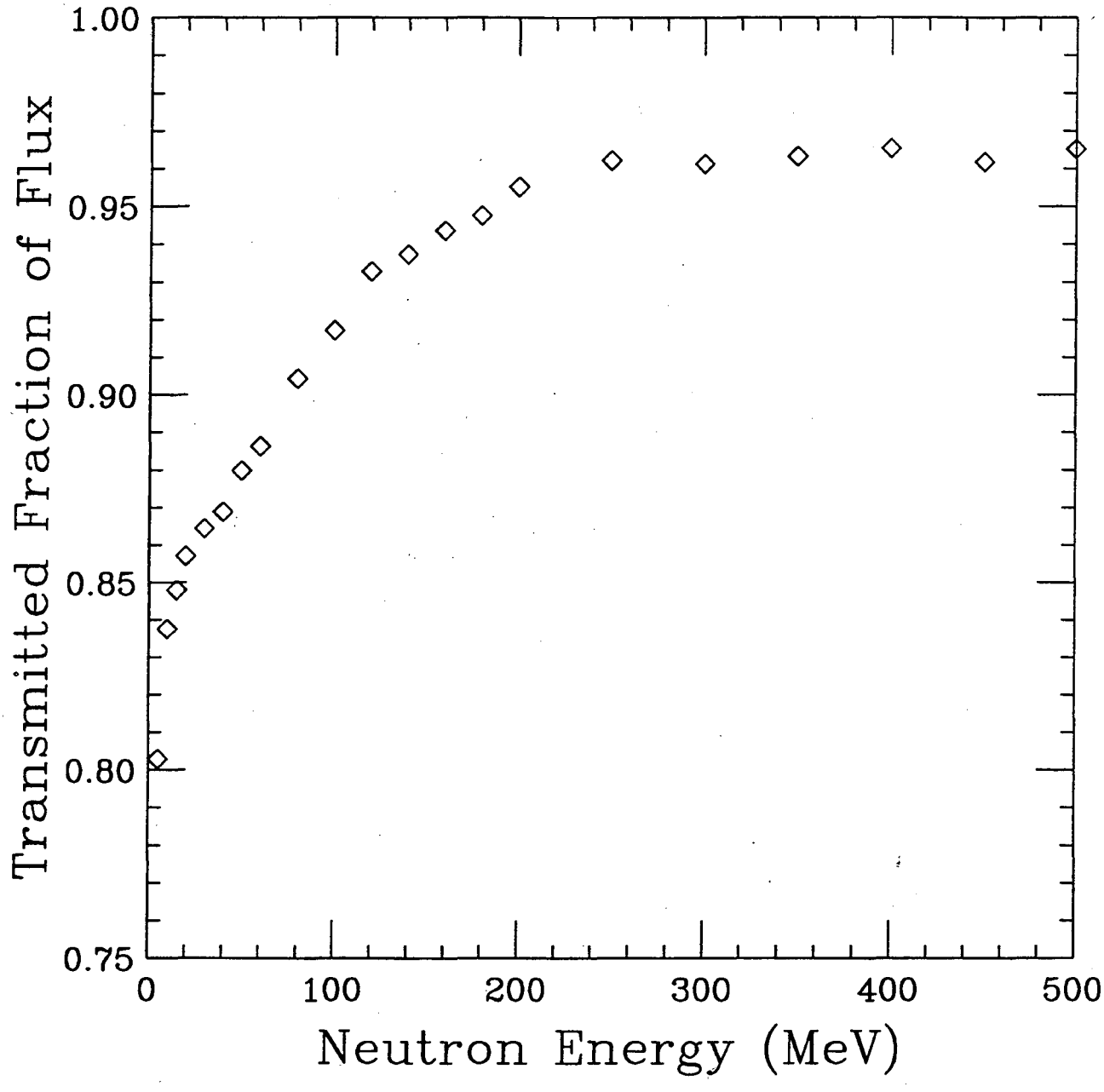

Fig. 5 - Fraction of the incident neutron flux transmitted to detector #9, as a function of energy. Flux lost is due to outscattering by materials between the target and the detector.

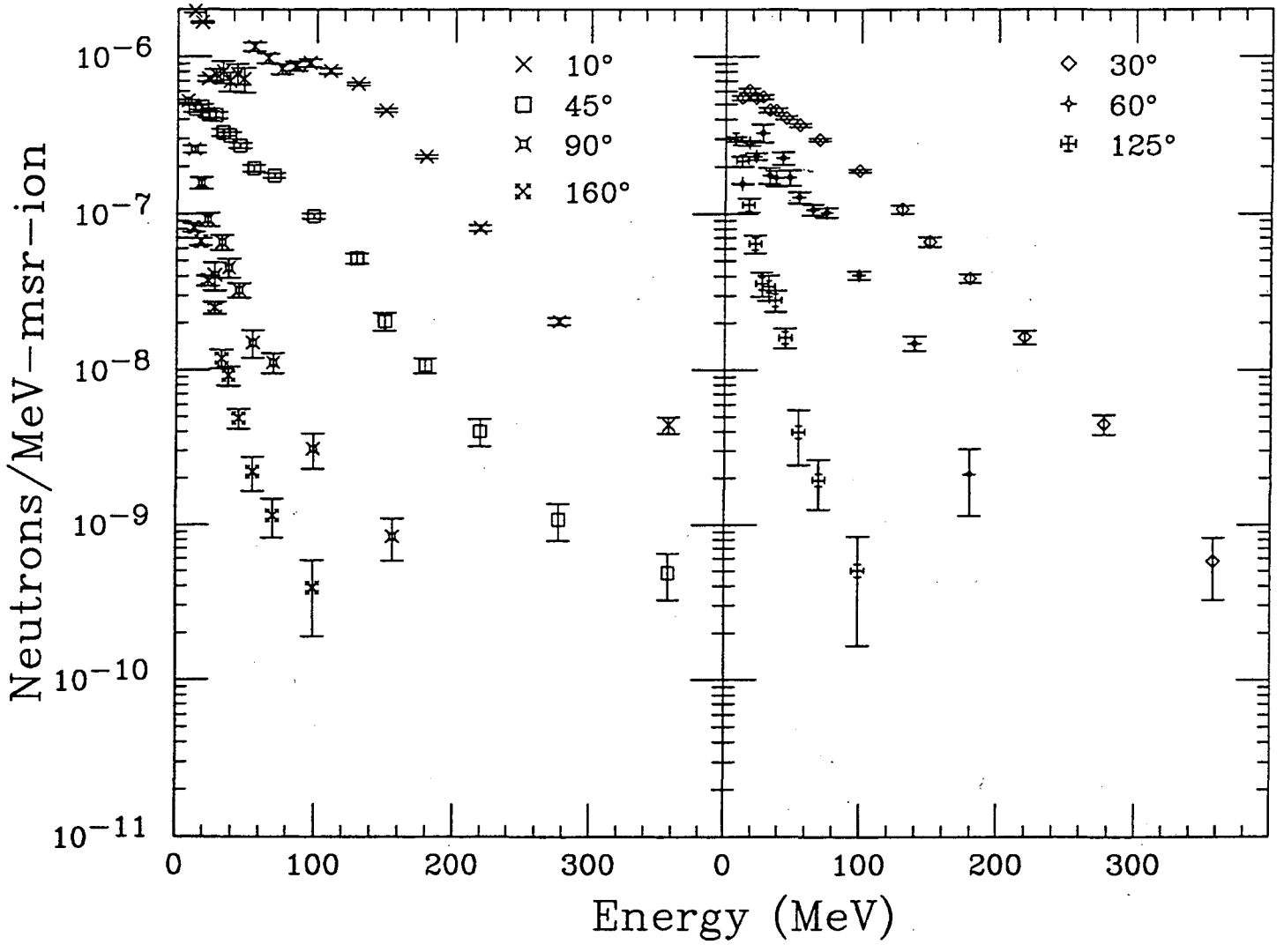

Fig. 6 - Double-differential spectra for the ^{12}C + Al system at 10°, 45°, 90°, 160° (left plot), and 30°, 60°, 125° (right plot).

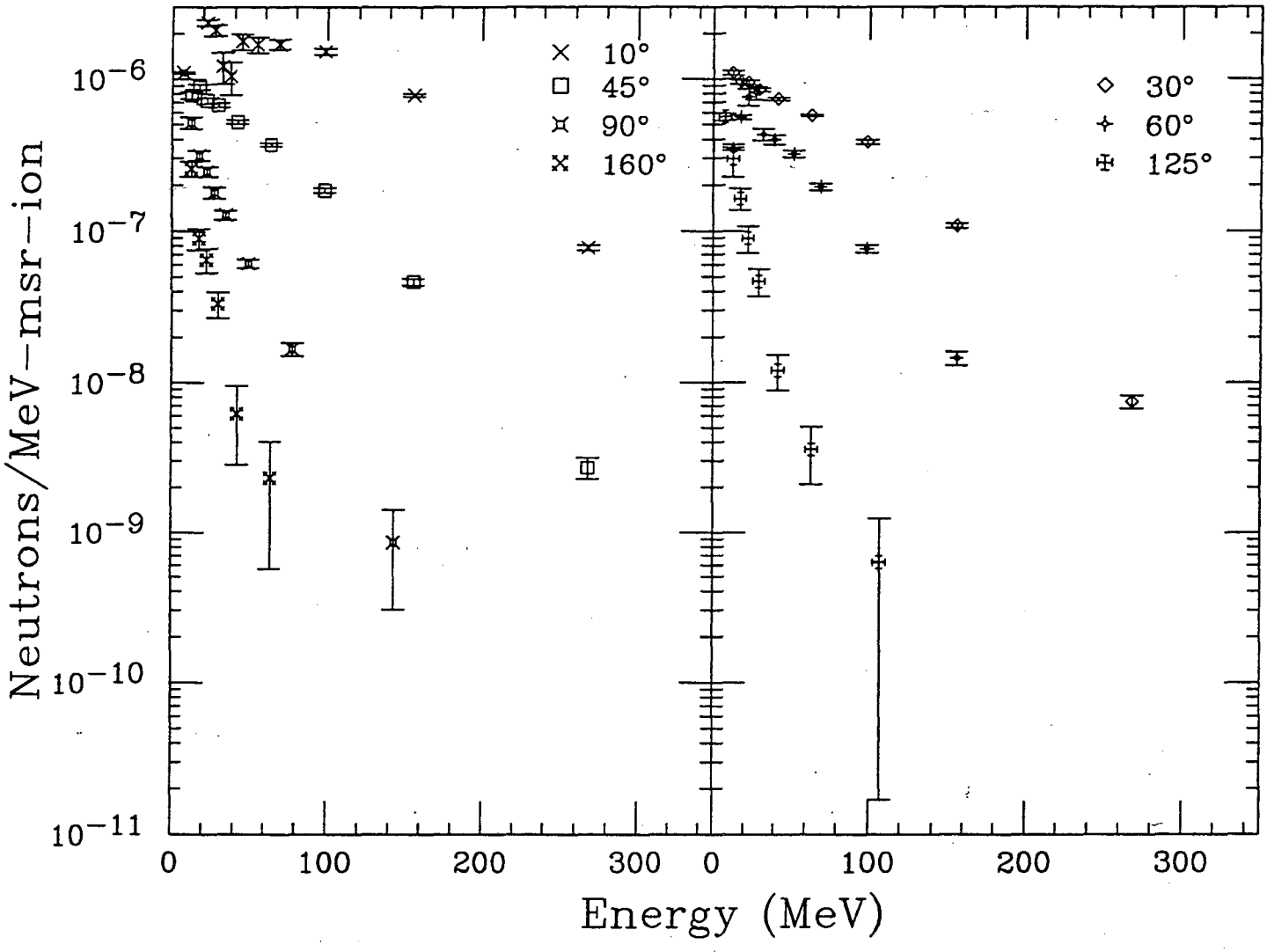

Fig. 7 - Double-differential spectra for the ^{4}He + Al system at 10°, 45°, 90°, 160° (left plot), and 30°, 60°, 125° (right plot).

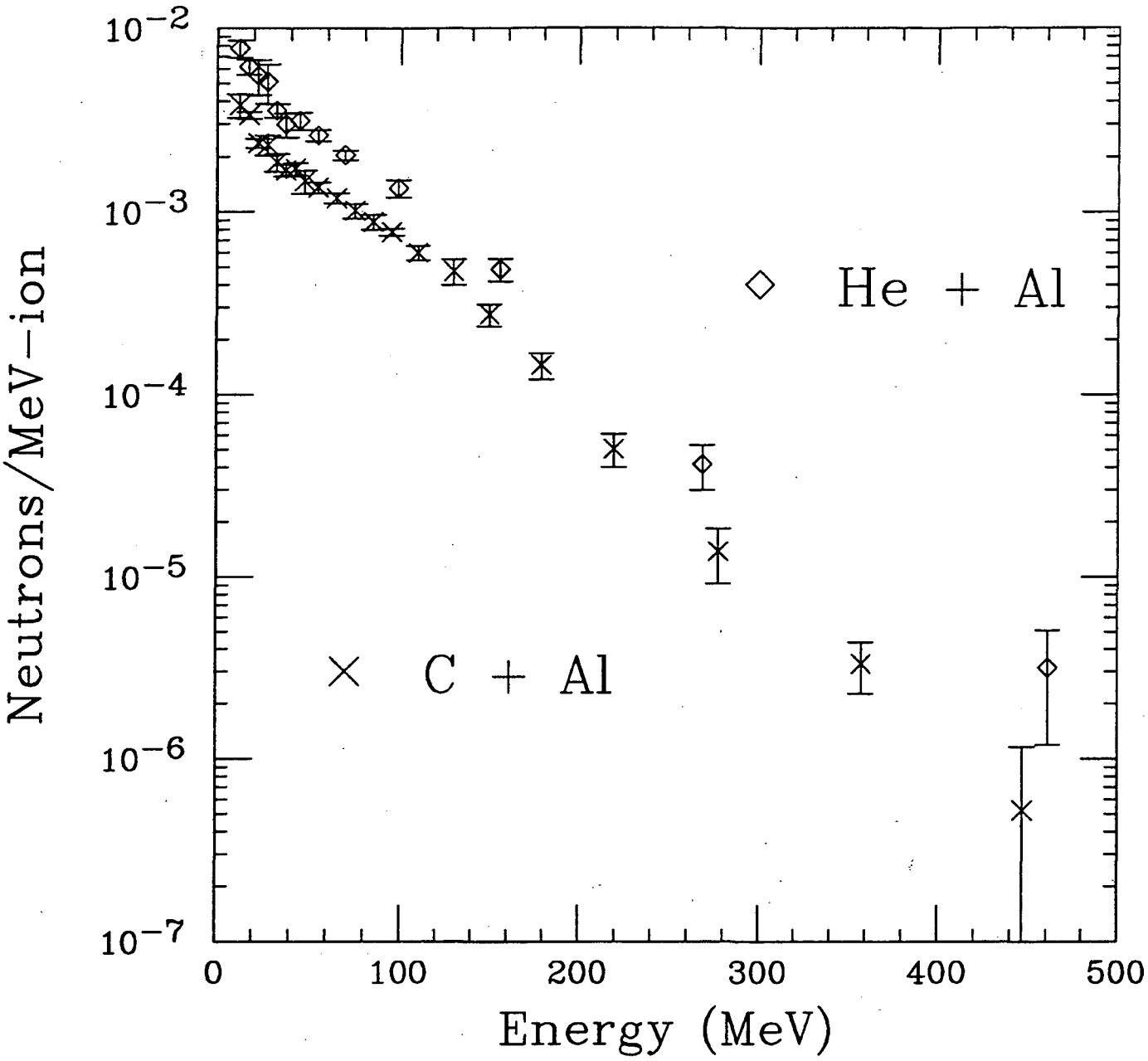

Fig. 8 - Energy distributions of the neutron yield for the ^{12}C + Al (X-shaped symbols) and ^{4}He + Al (diamond-shaped symbols) systems.

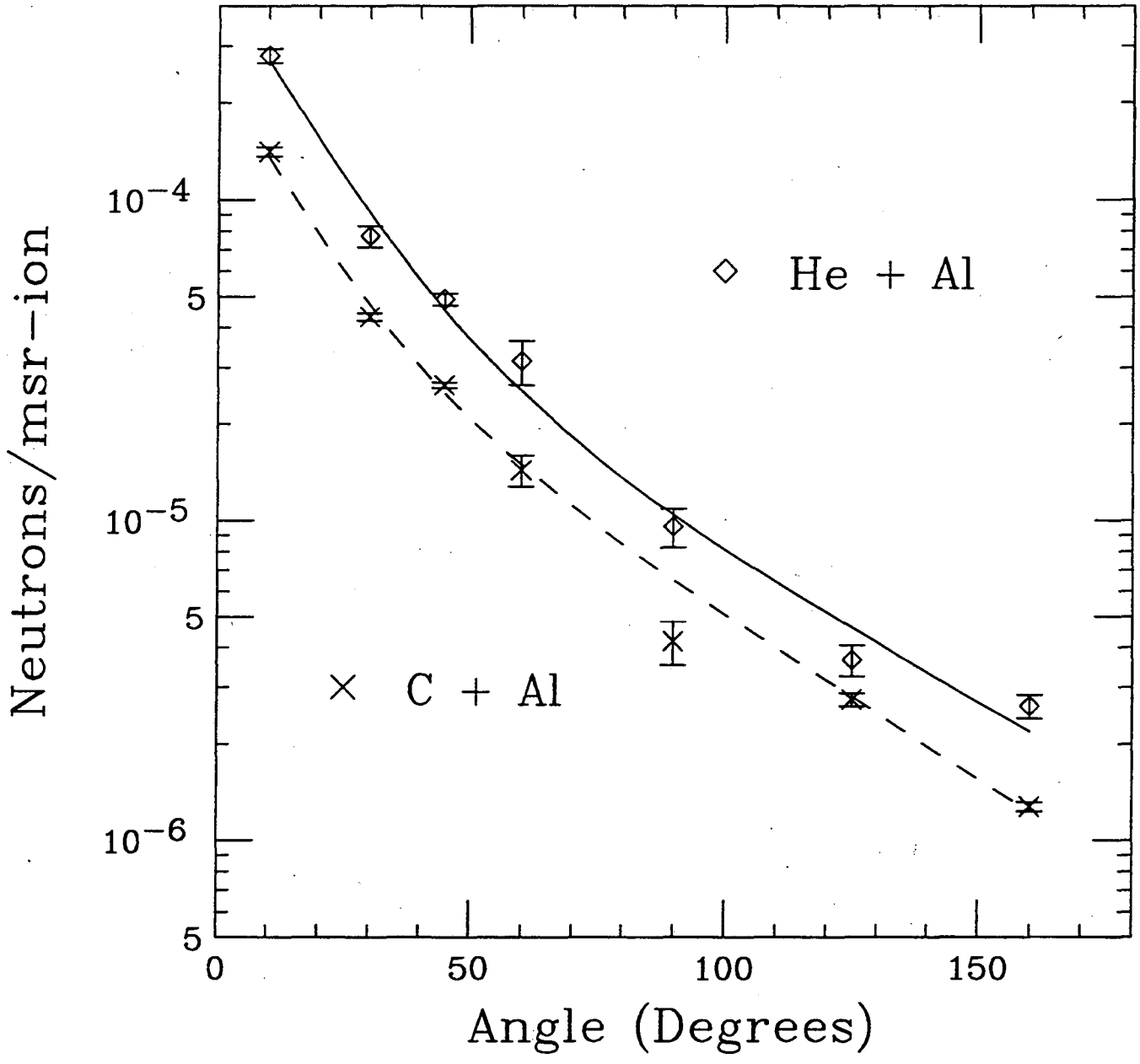

Fig. 9 - Angular distributions of the neutron yield for the ^{12}C + Al (X-shaped symbols) and ^{4}He + Al (diamond-shaped symbols) systems. The solid and dashed lines show fits to the data, as described in the text.

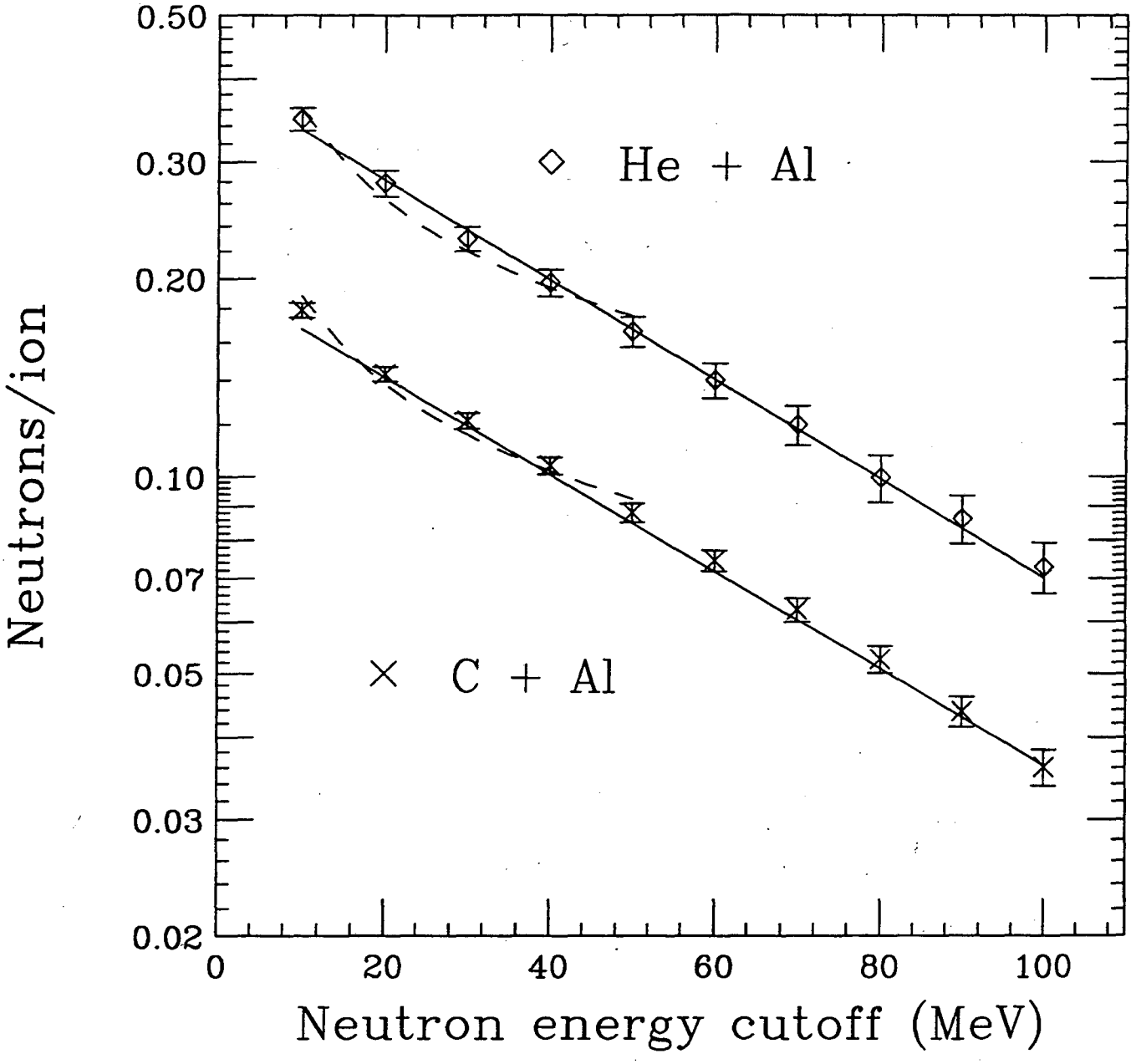

Fig. 10 - Total neutron yields above a given neutron energy for ^{4}He + Al (diamond-shaped symbols) and for ^{12}C + Al (X-shaped symbols). The dashed and solid lines come from fits explained in the text.

Ernest Orlando Lawrence Berkeley National Laboratory
One Cyclotron Road | Berkeley, California 94720

Prepared for the U.S. Department of Energy under Contract No. DE-AC03-76SF00098